Nonlin. Processes Geophys., 15, 881–891, 2008
www.nonlin-processes-geophys.net/15/881/2008/
© Author(s) 2008. This work is distributed under
the Creative Commons Attribution 3.0 License.

Nonlinear Processes in Geophysics

Influence of thresholding in mass and entropy dimension of 3-D soil images

A. M. Tarquis[1,2], R. J. Heck[3], J. B. Grau[2], J. Fabregat[2], M. E. Sanchez[2], and J. M. Antón[2]

[1]C.E.I.G.R.A.M. E.T.S. Ing. Agrónomos (E.T.S.I.A.), Universidad Politécnica de Madrid (U.P.M.), Ciudad Universitaria, s.n. 28040 Madrid, Spain
[2]Dpto. de Matemática Aplicada a la Ingeniería Agronómica. E.T.S. Ing. Agrónomos, U.P.M., Ciudad Universitaria, s.n. 28040 Madrid, Spain
[3]Department of Land Resource Science. Ontario Agricultural College, University of Guelph. NIG 2WI, Canada

Received: 10 April 2008 – Revised: 8 September 2008 – Accepted: 16 September 2008 – Published: 25 November 2008

Abstract. With the advent of modern non-destructive tomography techniques, there have been many attempts to analyze 3-D pore space features mainly concentrating on soil structure. This analysis opens a challenging opportunity to develop techniques for quantifying and describe pore space properties, one of them being fractal analysis.

Undisturbed soil samples were collected from four horizons of Brazilian soil and 3-D images at 45 μm resolution. Four different threshold criteria were used to transform computed tomography (CT) grey-scale imagery into binary imagery (pore/solid) to estimate their mass fractal dimension (D_m) and entropy dimension (D_1). Each threshold criteria had a direct influence on the porosity obtained, varying from 8 to 24% in one of the samples, and on the fractal dimensions. Linear scaling was observed over all the cube sizes, however depending on the range of cube sizes used in the analysis, D_m could vary from 3.00 to 2.20, realizing that the threshold influenced mainly the scaling in the smallest cubes (length of size from 1 to 16 voxels).

D_m and D_1 showed a logarithmic relation with the apparent porosity in the image, however, the increase of both values respect to porosity defined a characteristic feature for each horizon that can be related to soil texture and depth.

1 Introduction

Soil structure may be defined as the spatial arrangement of soil particles, aggregates and pores. The geometry of each one of these elements, as well as their spatial arrangement, has a great influence on the transport of fluids and solutes through the soil. Fractal geometry has been increasingly applied to quantify soil structure, using fractal parameters, due to the complexity of the soil structure, and thanks to the advances in computer technology (Tarquis et al., 2003, and references therein). The value of fractal parameters can be derived from indirect methods, such as water retention curves or directly through image analysis (Crawford et al., 1995).

For many years, two-dimensional (2-D) images of soil thin sections have been used in a number of endeavors to describe the spatial structure, extracting mass fractal dimension (D_m or D_0) and pore-solid interface (Brakensiek et al., 1992; Pachepsky, 1996; Giménez et al., 1997, 1998; Oleschko et al., 1997, 1998; Oleschko, 1998; Bartoli et al., 1999; Dathe et al., 2001; Dathe and Thulner, 2005) as spectral dimension (Anderson et al., 1996; Crawford and Matsui, 1996; Crawford et al., 1999). In the field of rock pore systems, Saucier (1992) related the effective permeability of the porous media with the entropy dimension (D_1) extracted from a 2-D image.

Several authors maintain that the exact value of the mass fractal dimension cannot be readily calculated (Crawford et al., 1999; Bird et al., 2006; Perrier et al., 2006). Tel and Vicsek (1987), for instance, proposed practical methods to compute it, indicating that the standard methods for determining fractal dimensions must be applied with some caution. The main difficulty is that the ideal limit cannot be reached in practice (Buczhowski et al., 1998). Moreover, there is an effect of the image manipulation on D_m and D_1 values (Babeye et al., 1998).

Computed tomography (CT) has provided an alternative for observing intact soil structure (Anderson et al., 1988; Warner et al., 1989; Grevers and Jong, 1994; Peyton et al., 1994; Perret et al., 1997, 1998, 1999, 2003; Rasiah and Aylmore, 1998a, b; Rogasik et al., 1999; Gantzer and Anderson,

Correspondence to: A. M. Tarquis
(anamaria.tarquis@upm.es)

Table 1. Physical properties of selected horizons of Argissol, as per Melo and dos Santos (1996).

Horizon	Depth	Consistency		Density (kg dm^{-3})		Particle Size Distribution (%)			
	(cm)	Dry	Moist	Bulk	Particle	C. Sand	F. Sand	Silt	Clay
A2	10–35	slightly hard	very friable	1.4	2.7	62	24	3	11
AB	35–57	slightly hard	friable	1.5	2.7	26	53	4	17
Bt2	98–152	slightly hard	friable	1.4	2.7	21	40	4	35
Bt/Bw	150–190	slightly hard	friable	1.3	2.7	18	37	10	35

2002; Pierret et al., 2002; Anderson et al., 2003; Rachmant et al., 2005; Gibson et al., 2006). The principal benefits of CT techniques are: reducing the physical impact of sampling, providing three-dimensional (3-D) information and allowing rapid scanning to study sample dynamics in near real-time (Rasiah and Aylmore, 1998b). Because of these benefits, CT scanning has been used to extract fractal dimensions related to soil structure. Peyton et al. (1994) evaluated the fractal dimension of macropore-scale density. Zeng et al. (1996) calculated fractal lacunarity in a silt loam soil. Several authors have dedicated their attention to the appropriate pore-solid CT threshold, before calculating mass fractal and surface fractal dimensions (Rogasik et al., 1999; Gantzer and Anderson, 2002; Perret et al., 2003; Rachmant et al., 2005). Recently, Gibson et al. (2006) compared three fractal analytical methods to quantify the heterogeneity within soil aggregates; in this work, the frequency distribution of pore and solid components was clearly dependent on thresholding, which could not be generalized.

As far as we know, they didn't quantify this effect on D_m and D_1. The aim of the present study is to evaluate the effect of the image thresholding value as well as the cube size on the calculation of mass fractal dimension (D_m) and entropy dimension (D_1). To this end, soil images from four horizons, obtained from a Brazilian Argissolo (Melo and dos Santos, 1996) were analyzed to obtain these fractal dimensions applying four different thresholds.

2 Materials and methods

2.1 Soil studied

Intact soil samples were collected from four horizons of an Argissolo in the Brazilian Soil Classification (EMBRAPA SOLOS, 2006), or Ultisol (FAO Soil Classification), formed on the Tertiary Barreiras group of formations in Pernambuco state (Itapirema Experimental Station) presenting a hardsetting behavior, found throughout the coastal tablelands of northeast Brazil. The natural vegetation of the region is tropical, coastal rainforest. Macromorphology and micromorphology, mineralogy, as well as key physical and characteristics of this soil, have been studied, from a genetic perspective, by Melo and dos Santos (1996). Physical characteristics, of relevance to the current study, are provided in Table 1.

2.2 CT imaging and image pre-treatment

The intact soil samples were imaged using an EVS (now GE Medical. London Canada) MS-8 MicroCT scanner. Though some samples required paring to fit the 64 mm diameter imaging tubes, field orientation was maintained. Imaging parameters were 155 keV and 25 μA.

Proprietary software (GE Medical), was used to reconstruct the 16-bit, 3-D imagery from the sequence of axial views. The resulting voxel size was 45.1 μm. File sizes ranged from 70 to 200 Mb, which made subsequent processing of the entire volume practically impossible. Accordingly, one subvolume was extracted from each of the four original volumes (using GE Medical Microview); care was taken to ensure no edged effect of the subvolume. The subvolumes measured $256\times256\times256$ units, corresponding to about 16.8 million voxels. A 3-D Gaussian filter in MicroView (GE Healthcare, 2006) was also run on each sub-volume to reduce noise, typical of CT imagery. An example of a typical 3-D imagery is provided in Fig. 1.

2.3 Binary thresholding of CT imagery

CT imagery of soil, like other digital imagery, typically contains a large proportion of mixed-voxels (voxels whose digital number is the weighted average of more than one constituent – such as a solid/air interface). To facilitate identification of constituent peaks in the grey-scale histogram, a 3-D filter, executed in NIH ImageJ (Rasband, 2006) was run on each sub-volume to mask voxels which differed by more than 0.1% from the surrounding neighborhood of 124 voxels ($5\times5\times5$ unit volume). Full details of this technique can be found in Elliot and Heck (2007). Histograms of the unmasked voxels were subsequently ported into OriginPro (Origin Lab Corporation, 2006); after smoothing the histograms (adjacent averaging of 25 levels), peaks were identified in the Peak Fitting Module. The major peak with the lowest mean digital number was taken to be that corresponding to the void space; the next major peak was considered to be solid material. Based on the central tendency and dispersions (assuming Gaussian distributions) of the two peaks,

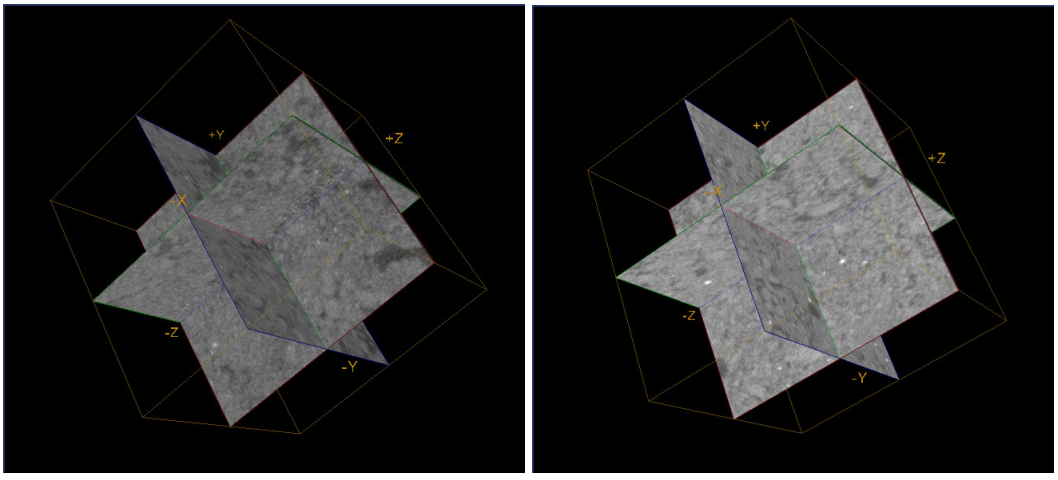

A2 AB

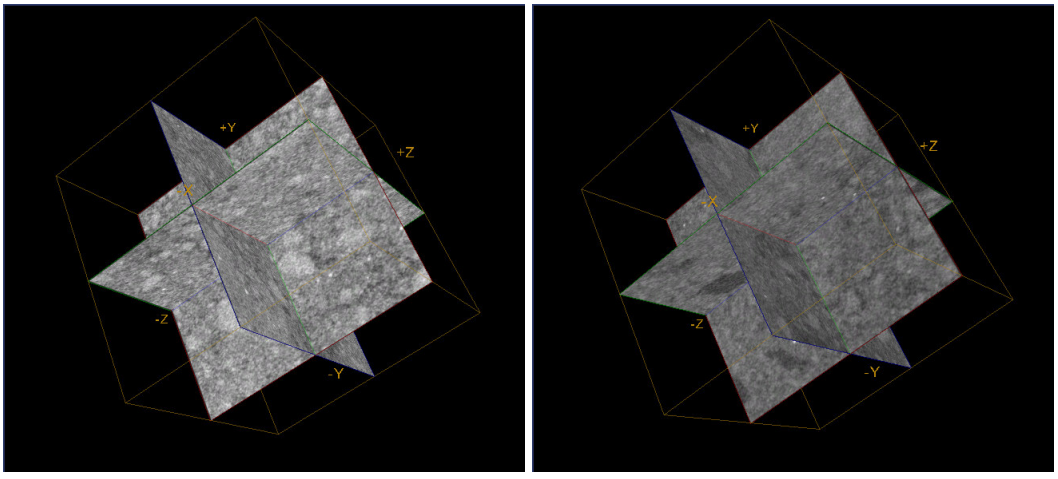

Bt2 Bt/Bw

Fig. 1. Typical grey-scale CT imagery (orthogonal planes) of sub-volumes for each of the horizons studied. Dark regions correspond to less attenuating regions (pores), lighter areas to solid components. Z-axis is vertical, with $Z+$ representing top of sample. Length of edge of cube is 11.54 mm.

four threshold values were identified (Fig. 2): a) lower 3rd standard deviation of solid (low probability containing solid); b) central tendency for air (μ_{CTair}); c) equi-probability value for air and solid and d) mean of the central tendencies for air and solid. Thresholds B and C are the most commonly used in soil science beside a subjective choice comparing the original and binary image by the experts, which we refuse to use in this study. Thresholds A and D were selected to have a total of four values to clearly study their influence on the fractal dimensions.

2.4 Mass fractal dimension

The binarized image is considered to represent two basic phases: pores and solid. Fractal analysis (FA) in 3-D images involves partitioning the space into cubes to construct samples and recording the number of cubes which cover the pores phase; this is repeated for different size cubes (Perret et al., 2003).

The cube-counting (CC), similar to the box-counting method in 2-D, combines voxels to form larger, mutually exclusive cubes each containing a different set of voxels. Given an $L\times L\times L$-voxel image, partitioned to a cube size of $\delta\times\delta\times\delta$, the number of cubes ($n(\delta)$) will follow the proportion of line size δ:

$$n(\delta) \propto \left(\frac{L}{\delta}\right)^3 \quad (1)$$

If δ is overly large, the resulting number of samples is lower. At each scale (δ) the number of cubes of size δ with at least

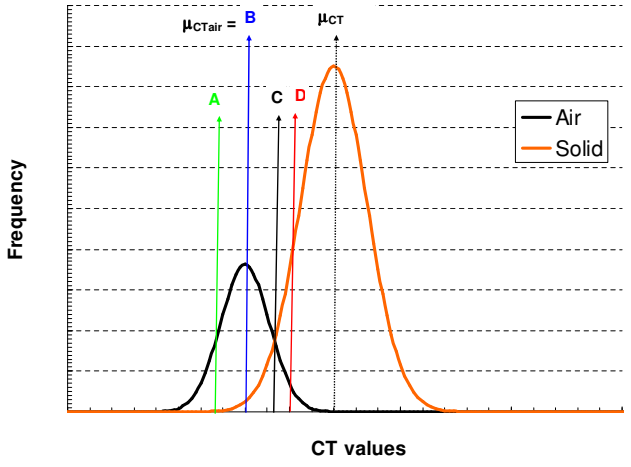

Fig. 2. Graphical representation of the different thresholding criteria, used to binarize the frequency distribution of CT values: A – CT value corresponding to 0.01% distribution of the CT values distribution of solid, B – mean of CT values of air (μ_{CTair}), C – equi-probability CT values of air and solid and D – average of mean CT values of air (μ_{CTair}) and mean CT values of solid (μ_{CTsolid}).

one pixel belonging to the pore space ($N(\delta)$) is recorded. Being $N_j(\delta)$ the number of cubes of size δ with j pixels belonging to the pore space (with a value from 1 to $\delta\times\delta\times\delta$):

$$N(\delta) = \sum_{j=1}^{\delta^3} N_j(\delta) \tag{2}$$

For a fractal set a log-log plot of $N(\delta)$ vs. δ gives:

$$N(\delta) \propto \delta^{-D_m} \tag{3}$$

which yields a line of slope equal to $-D_m$; being D_m the mass fractal dimension. It is expected that, as the object fills the space in 3-D, D_m will approach the Euclidean dimension (E) of three.

Given the relation (1) it is now instructive to seek bounds on the values the function $N(\delta)$ can take based on Bird et al. (2006) work. We denote the fraction of the image occupied by pore phase at the finest resolution (i.e. porosity) by p. If p=1 the number of cubes required to cover the set is $\left(\frac{L}{r}\right)^2$ and this is trivially an upper bound for $N(\delta)$ when $p<1$. In order to derive a lower bound, we consider the situation in which the cubes cover the set but no part of the complementary set. If this were to occur, then the number of cubes is equal to $\left(\frac{L}{r}\right)^2 f$. In general, the cubes will cover part of the complementary set and consequently the former number of cubes is a lower bound for $N(\delta)$. We may now write that $N(\delta)$ must satisfy the inequalities:

$$\left(\frac{L}{r}\right)^2 f \le N(r) \le \left(\frac{L}{r}\right)^2 \tag{4}$$

In terms of the log-log plot used to extract a mass fractal dimension, these inequalities result in two parallel reference

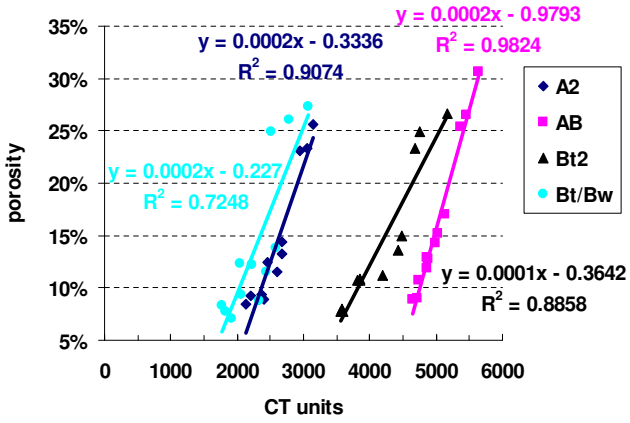

Fig. 3. Soil porosity versus CT units of threshold for each horizon and sub-volume. Linear fits for each horizon represents the change of porosity per CT unit.

lines of slope −3, between which the measured data must lie. The vertical spacing between these lines is equal to $\log(p)$. For all images sharing a common value of p, the cube counting data will lie between these bounding lines. Analytically, we can conclude that the higher the porosity, the closer the boundary lines are and then D_m value will be closer to 3.

2.5 Entropy dimension

This calculation in 3-D imagery involves partitioning the space into cubes to construct samples with multiple scales. The cube-counting method (CC), similar to box-counting method in 2-D, combines voxels to form larger, mutually exclusive cubes each containing a different set of voxels. Given an $L\times L\times L$-voxel image, partitioned to a cube grid of size $\delta\times\delta\times\delta$, the fraction of pore space (μ_i) in each $n(\delta)$ cubes (density) is calculated from:

$$\mu_i = \frac{m_i}{m_T} = \frac{m_i}{\sum_{i=1}^{n(\delta)} m_i} \tag{5}$$

where m_i is the number of pore class voxels in cube i, and m_T is the total number of pore class voxels in an image. In this case, the pore density is the measure and the cube grid the support. When computing the number of cubes of size δ, the possible values of m_i range from 0 to $\delta\times\delta\times\delta$. So, if $N_j(\delta)$ is the number of cubes containing j voxels of pore volume in a given grid, Eqs. (4) and (5) can then be combined (Barnsley et al., 1988):

$$\sum_{i=1}^{n(\delta)} \mu_i(\delta) = \sum_{i=1}^{n(\delta)} \left(\frac{m_i}{m_T}\right) = \sum_{j=1}^{\delta^3} N_j(\delta) \left(\frac{j}{m_T}\right) \tag{6}$$

where: $m_T = \sum_{j=1}^{\delta^3} j\, N_j(\delta)$.

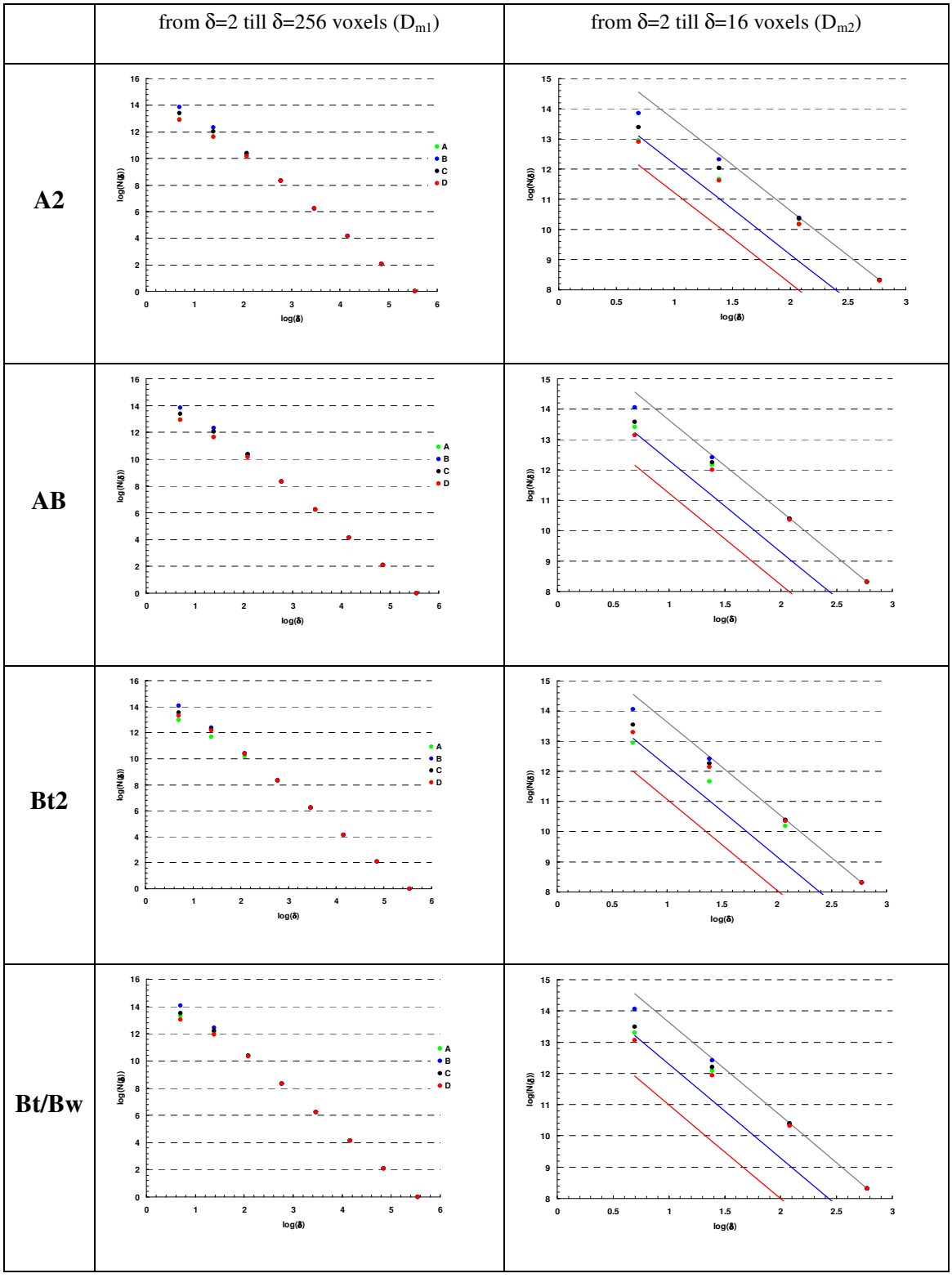

Fig. 4. Log-log plot of $N(\delta)$ versus cube size (δ) at different threshold values for each horizon and sub-volume a. Left columns shows all the size range, right column shows from δ=2 till δ=16 voxels. Gray line is the maximum line boundary, blue and red lines are the minimum line boundary respectively for B and D threshold values.

Table 2. Threshold values obtained applying different methods: A) CT value that represent the 0.1% of the CT values distribution corresponding to solid; B) average of CT values corresponding to air; C) intersection point of frequency distribution of CT values corresponding to air and solid and D) mean of average CT values corresponding to air and average CT values corresponding to solid.

Horizon	Subvolume	Threshold values			
		Lower 3rd solid standard dev. (A)	Air mean (B)	Air & solid equi-probability (C)	Average of means for air & solid (D)
A2	a	2336	2370	2681	3047
	b	2126	2210	2464	2940
	c	2397	2597	2682	3148
AB	a	4717	4865	4987	5466
	b	4644	4737	4876	5376
	c	4854	5029	5134	5639
Bt2	a	3595	3552	3855	4679
	b	4193	4421	4481	5165
	c	3578	3818	3842	4746
Bt/Bw	a	1916	2055	2218	2775
	b	2335	2447	2589	3070
	c	1825	1777	2043	2521

By using the distribution function $N_j(\delta)$ it simplifies calculations and reduces computational errors (Barnsley et al., 1988). The entropy of the system is estimated through this dimension by the relation (Feder, 1989):

$$D_1 = \lim_{\delta \to 0} \frac{\sum_{i=1}^{n(\delta)} \mu_i(\delta) \log[\mu_i(\delta)]}{\log \delta} = \lim_{\delta \to 0} \frac{S(\delta)}{\log \delta} \quad (7)$$

The higher the D_1 is, the lower the information (higher uncertainty) we have on the distribution of pore/solid fractions achieving a higher homogeneity. Contrary, the lower the values of D_1, the more information (lower uncertainty) we have on this distribution and then lower homogeneity.

The lower and upper limits of $S(\delta)$ were calculated in function of the porosity (p) for 3-D binary images given:

$$3 \ln\left(\frac{L}{\delta}\right) + \ln(p) < -\sum_{i=1}^{n(\delta)} \mu_i \ln(\mu_i) < 3 \ln\left(\frac{L}{\delta}\right) \quad (8)$$

the bounding functions when included on the plot of entropy against $\ln(\delta)$ again yield two parallel lines of slope 3, with separation of $\ln(p)$. The higher the porosity, the closer the two boundaries and D_1 will approach 3.

3 Results and discussion

3.1 Thresholding methods

As indicated in Table 2, the mean of the modal values for the air and solid distributions consistently resulted in the largest thresholding values, followed by the equi-probability value for the two distributions. Though the thresholding values corresponding to the other two criteria were consistently lower than those obtained from both distributions, there was no consistent trend between the air mean and the lower 3rd standard deviation of the solid distributions. A variation of specific thresholding values, among subvolumes of a given sample, suggests the high variability in the intensity field obtained from the CT scan. As indicated in Fig. 3, apparent porosity was more sensitive to the selected thresholding criteria in the Bt/Bw horizons than for the A2 and AB horizons, which followed a more linear trend. However, Bt/Bw is less sensitive to thresholding criteria than the Bt2 horizon.

3.2 Mass fractal dimension

For all horizons, the porosity obtained varied as a function of the threshold method applied (Table 3). As expected, threshold method D gave the higher porosity, from 24% for the A2 horizon to 28% for the AB horizon, and threshold method A gave the lowest, from 8% for the Bt/Bw horizon to 10% for the AB horizon. In all cases, we obtain statistically significant straight-line fits (R^2>0.98) for the full range of box sizes considered (from 1 to 256 voxels) as it is shown in Table 3 (D_{m1}). The mass fractal dimensions derived from these calculations are very close to 3, with the lowest being 2.70 for A2 horizon using threshold method A, and the highest 2.94 for horizons AB, Bt2 and Bt/Bw, when applying method D. Comparing among horizons (Table 3), the A2 horizon always exhibited the lowest value in D_m and Bt2 the highest value, regardless of the thresholding method.

Table 3. Average (three replicates) porosity and mass dimension (D_m) for each horizon and thresholding criteria based on a range from δ=2 till δ=256 voxels (D_{m1}) and from δ=2 till δ=16 voxels (D_{m2}). For all linear fits the R^2 obtained was higher than 0.98.

Horizon	Threshold	Porosity	±s.e.	D_{m1}	R^2	D_{m2}	R^2
A2	A	8.749	0.003	2.703	0.994	2.222	0.993
	B	10.013	0.013	2.734	0.999	2.670	0.995
	C	13.348	0.010	2.798	0.997	2.439	0.992
	D	23.966	0.014	2.900	0.994	2.202	0.993
AB	A	10.253	0.023	2.797	0.996	2.833	0.996
	B	12.594	0.024	2.834	0.999	2.933	0.999
	C	14.729	0.021	2.859	0.997	2.861	0.997
	D	27.515	0.028	2.935	0.995	2.786	0.995
Bt	A	8.950	0.019	2.838	0.996	2.222	0.993
	B	10.661	0.029	2.856	0.999	2.776	0.997
	C	12.139	0.024	2.872	0.997	2.534	0.990
	D	24.978	0.017	2.940	0.996	2.409	0.985
Bt/Bw	A	7.871	0.009	2.800	0.996	2.397	0.987
	B	9.741	0.017	2.823	0.999	2.776	0.997
	C	12.765	0.009	2.864	0.997	2.504	0.990
	D	26.086	0.012	2.939	0.994	2.280	0.985

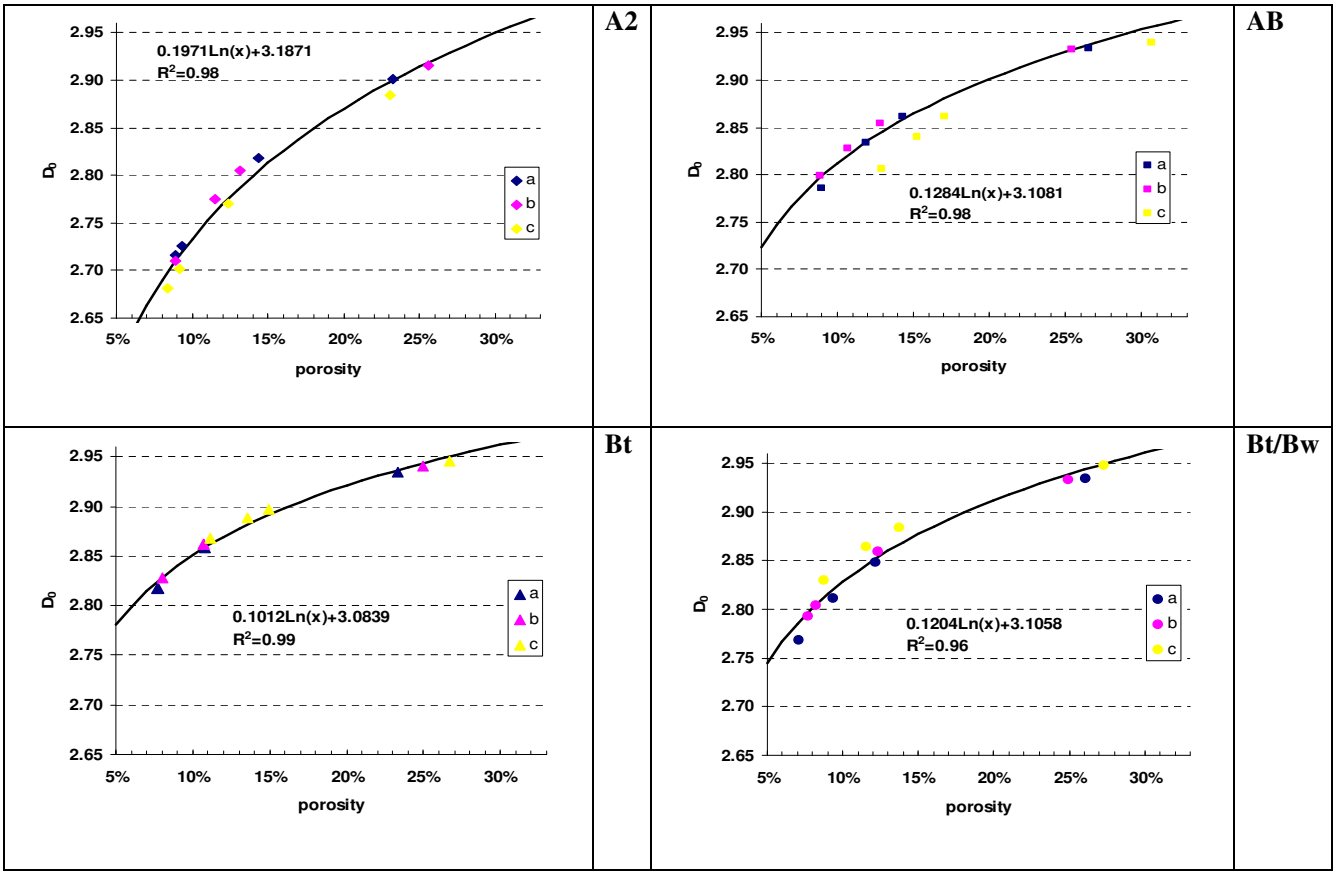

Fig. 5. Mass fractal dimension (D_m) versus porosity for each horizon and sub-voxel. Logarithmic regression lines and their corresponding equation are included in each graphic.

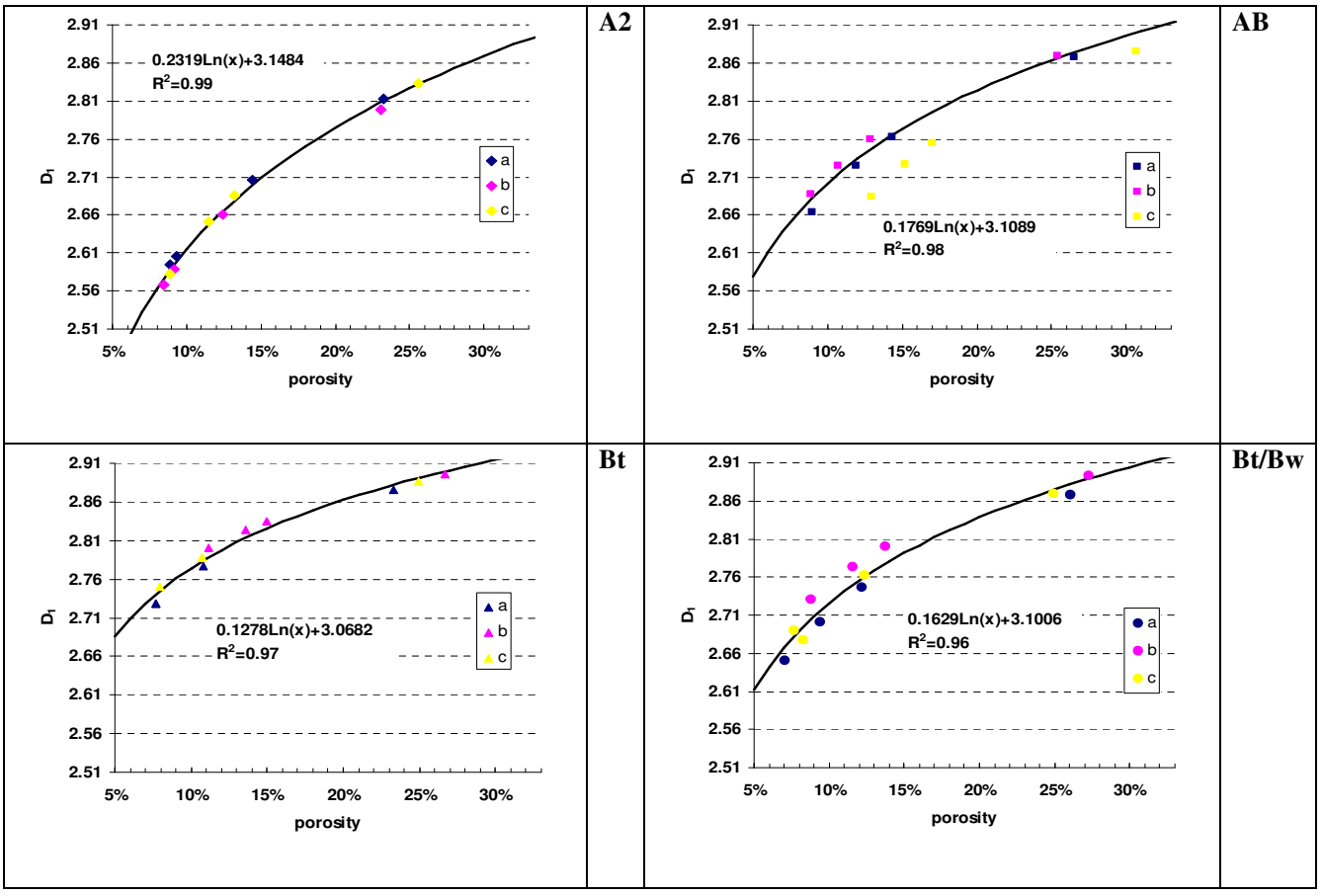

Fig. 6. Entropy fractal dimension (D_1) versus porosity for each horizon and sub-voxel. Logarithmic regression lines and their corresponding equation are included in each graphic.

In order to closely examine the relationship between porosity and mass fractal dimension, a bi log plot of $N(\delta)$ and δ is shown in more detail (Fig. 4). It is now apparent that soil porosity is mainly affecting the smallest voxels from length size δ=2 to 16 that influence the D_m value obtained. If we reduce our estimation of D_m to this size range (D_{m2}) values are lower and show more variation (Table 3). From now on, we will use only D_{m1} and named it as D_m.

At the highest porosity values (Table 3), the differences in D_m among the horizons are much smaller than at the lowest values. Moreover, it was observed that, for each horizon, the trend was not linear, but rather showed several increments that can be fitted by a logarithmic curve. To study this observation closer, several plots were done to see the variation of D_m versus porosity for each horizon and sub-voxel (Fig. 5). What can easily be seen is that for a certain horizon it didn't matter what the porosity for each sub-voxel and threshold was, all of them follow a pattern. This pattern is different depending on the horizon. In the case of the horizon AB, sub-voxel *c* is different from the other two, highlighting a possible problem in the image due to a beam hardening effect that was verified. For this reason, we didn't include sub/voxel *c* in the logarithmic regression for this horizon.

Comparing these results to the particle size distribution (PSD) and depth for each horizon (Table 1), it can be observed that the most superficial one (A2) and with higher coarse sand percentage (62%) presents the steepest curve with respect to porosity (Fig. 5). Next horizon, AB, reduces the curve convexity as it shows a reduction to 26% of coarse sand and its depth (lower than 35 cm) protect it from any tillage practice. With the last two horizons, the clay percentage increases to double (35%) and has a low percentage in coarse sand. The curves of D_0 versus porosity are quite close and show the lower coefficients values multiplying Ln(porosity).

3.3 Entropy and correlation dimension

After calculating $S(\delta)$ for all binary images, it was plotted against log(δ); a clear linear pattern was observed in all plots (data not shown). The same comments that we have made for D_m could be applied here too. Table 4 shows the results obtained from function of soil horizon and threshold applied.

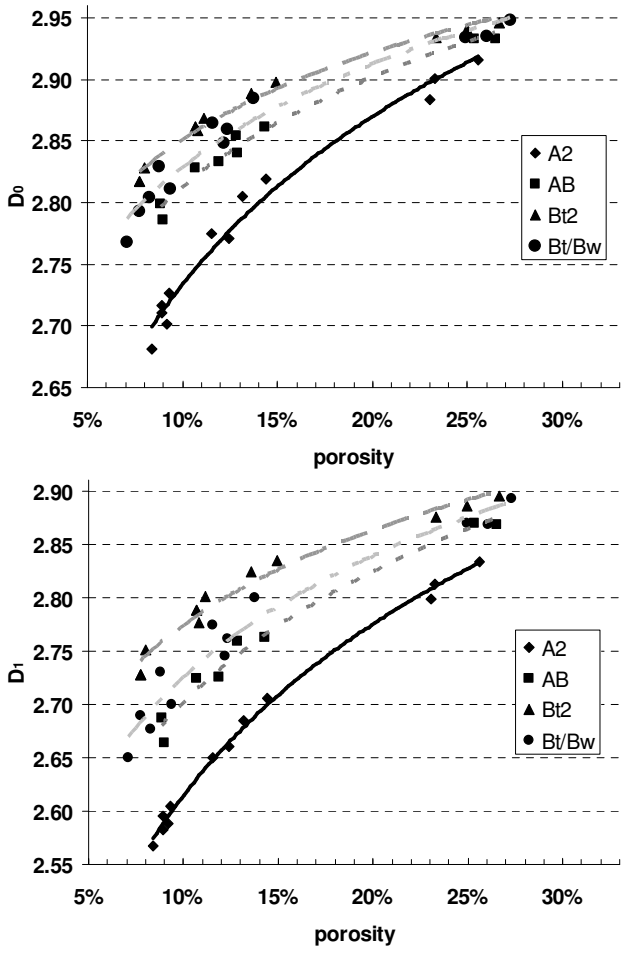

Fig. 7. Mass fractal dimension (D_m) and entropy fractal dimension (D_1) versus porosity for each horizon. Horizon AB is represented only by sub-voxels *a* and *b*.

The higher the threshold value (from A to D), the higher the porosity and D_1 increases approaching the value of 3 and the s.e. decreases. At threshold D all D_1 are higher than 2.90, pointing out a high homogeneity. As we did for mass dimension, we plotted D_1 for each horizon versus the porosity of the soil at that threshold value (Fig. 6) realizing again that each sub-voxel differs in the porosity and D_1 associated, the three of them varies D_1 similarly when the threshold is pushed forward. For example, this trend for horizon A2 is much more linear for D_1 case than for D_m values. At the same time, AB shows a big difference in sub-voxel *c* with respect to sub-voxel *a* and *b*.

Once these fractal dimensions versus porosity have been analyzed, all the horizons are plotted together for D_1 and D_m (Fig. 7). In both it is clear that A2 shows a very distinctive trend more than the other three horizons pointing out the influence of a high percentage of coarse sand and being the most superficial horizon that can be affected by tillage practices. Horizon Bt2 shows the minimum slope in variations of D_m and D_1 versus the porosity and therefore, versus threshold, similarly with low content in coarse sand, low content in silt and 35% in clay. AB and Bt/Bw are inside the area marked by the other two horizons. Bt/Bw has the lowest content in coarse sand (18%), a higher content in clay (35%) as Bt2 but higher content in silt compared with the rest of the horizons (10%).

Table 4. Entropy dimension (D_1), average of each horizon based on the three replicates applying four different threshold values.

Horizon	Threshold	$D_1 \pm$s.e.	
A2	A	2.699	0.033
	B	2.739	0.036
	C	2.809	0.021
	D	2.910	0.011
AB	A	2.876	0.076
	B	2.904	0.060
	C	2.920	0.051
	D	2.969	0.016
Bt2	A	2.915	0.013
	B	2.921	0.016
	C	2.929	0.007
	D	2.958	0.003
Bt/Bw	A	2.846	0.057
	B	2.859	0.066
	C	2.898	0.037
	D	2.957	0.015

4 Conclusions

3-D CT images from undisturbed soil samples were obtained from four horizons and three adjacent positions, having a total set of 12 samples. In order to describe the porosity structure, four threshold values were applied to convert each image into binary and then calculate D_m and D_1 as a quantification of soil morphology.

The sensitivity of each horizon to the threshold value on porosity was revealed indicating the differences in the CT unit values histogram among horizons although with these types of analyses, results cannot reflect the space arrangement of pores.

Linear scaling was observed over all the cube sizes for both fractal dimensions, however depending on the range of cube sizes used in the linear regression, the values obtained changed. For example, in one of the images D_m could vary from 3.00 to 2.20. Observing the log-log plots to estimate the dimensions, we conclude that threshold influenced mainly the scaling in the smallest cubes (length of size from 1 to 16 voxels).

D_m and D_1 showed a logarithmic relation with the apparent porosity in the image for the 12 samples studied. Plotting all the data of porosity and its D_m or D_1 independently of the threshold applied, the increase of both with respect to porosity defining a characteristic feature for each horizon that indirectly differentiate their structures. These differences can be explained based on the texture and depth of each horizon. These D_m variations are in agreement with the functional box-counting concept presented by Lovejoy et al. (1987) to extract the multiple dimensions of multiscale fields. Further research is necessary to present a wider variability in soil texture and applying this type of analysis so a statistical analysis can be made in order to estimate these relationships. However, from these results we can conclude that the higher the porosity, the harder it is to differentiate the differences in D_m and D_1 among horizons.

This indicates that fractal/multifractal analysis of the CT unit values could be applied to be able to choose an optimal thresholding as it is already used in many areas of geoscience.

Acknowledgements. Second author acknowledges the Canadian Foundation for Innovation and Ontario Innovation Trust for providing funding to acquire the micro-CT scanning system, as well as EVS (now GE Medical) of London, Canada for designating micro-CT laboratory as Luminary Site. The funding of Madrid Autonomous Community (CM) under projects number M070020163 and M0800204139 is greatly appreciated.

Edited by: Q. Cheng
Reviewed by: X. Deyi, K. Oleschko, and two other anonymous referees

References

Anderson, S. H., Gantzer, C. J., Boone, J. M., and Tully, R. J.: Rapid nondestructive bulk density and soil-water content determination by computed tomography, Soil. Sci. Soc. A. J., 52, 35–40, 1988.

Anderson, A. N., McBratney, A. B., and FitzPatrick, E. A.: Soil Mass, Surface, and Spectral Fractal Dimensions Estimated from Thin Section Photographs, Soil. Sci. Soc. A. J., 60, 962–969, 1996.

Anderson, S. H., Wang, H., Peyton, R. L., and Gantzer, C. J.: Estimation of porosity and hydraulic conductivity from x-ray CT-measured solute breakthrough, in: Applications of X-ray Computed Tomography in the Geosciences, edited by: Mees, F., Swennen, R., Van Geet, M., and Jacobs, P., p. 135–149, Geological Society of London Spec. Pub. 215, Geological Society of London, London, 2003.

Barnsley, M. F., Devaney, R. L., Mandelbrot, B. B., Peitgen, H. O., Saupe, D., and Voss, R. F.: The Science of Fractal Images, edited by: Peitgen, H. O. and Saupe, D., Springer-Verlag, New York, 66–67, 1988.

Bartoli, F., Bird, N. R., Gomendy, V., Vivier, H., and Niquet, S.: The relation between silty soil structures and their mercury porosimetry curve counterparts: fractals and percolation, Eur. J. Soil Sci., 50, 9–22, 1999.

Baveye, P., Boast, C. W., Ogawa, S., Parlange, J. Y., and Steenhuis, T.: Influence of image resolution and thresholding on the apparent mass fractal characteristics of preferential flow patterns in field soils, Water Resour. Res., 34, 2783–2796, 1998.

Bird, N., Díaz, M. C., Saa, A., and Tarquis, A. M.: A Review of Fractal and Multifractal Analysis of Soil Pore-Scale Images, J. Hydrol., 322, 211–219, 2006.

Brakensiek, D. L., Rawls, W. J., Logsdon, S. D., and Edwards, W. M.: Fractal description of macroporosity, Soil Sci. Soc. Am. J., 56, 1721–1723, 1992.

Buczhowski, S., Hildgen, P., and Cartilier, L.: Measurements of fractal dimension by box-counting: a critical analysis of data scatter, Physica A, 252, 23–24, 1998.

Crawford, J. W. and Matsui, N.: Heterogeneity of the pore and solid volume of soil: distinguishing a fractal space from its non-fractal complement, Geoderma, 73, 183–195, 1996.

Crawford, J. W., Baveye, P., Grindrod, P., and Rappoldt, C.: Application of Fractals to Soil Properties, Landscape Patterns, and Solute Transport in Porous Media, in: Assessment of Non-Point Source Pollution in the Vadose Zone, Geophysical Monograph, 108, edited by: Corwin, D. L., Loague, K., and Ellsworth, T. R., American Geophysical Union, Wahington, D.C., p. 151, 1999.

Crawford, J. W., Matsui, N., and Young, I. M.: The relation between the moisture-release curve and the structure of soil, European J. of Soil Sci., 46, 369–375, 1995.

Dathe, A., Eins, S., Niemeyer, J., and Gerold, G.: The surface fractal dimension of the soil-pore interface as measured by image analysis, Geoderma, 103, 203–229, 2001.

Dathe, A. and Thulner, M.: The relationship between fractal properties of solid matrix and pore space in porous media, Geoderma, 129, 279–290, 2005.

Elliot, T. R. and Heck, R. J.: A comparison of 2D and 3D thresholding of CT imagery, Can. J. Soil Sci., 87(4), 405–412, 2007.

EMBRAPA SOLOS: Sistema de Clasificačao de Solos, 2a Edičao, Empresa Brasileira de Pesquisa Agropecuaria, Solos, Rio de Janeiro, 306 pp, 2006.

Feder, J.: Fractals, Plenum Press, New York, p. 83–84, 1989.

Gantzer, C. J. and Anderson, S. H.: Computed tomographic measurement of macroporosity in chisel-disk and no-tillage seedbeds, Soil Tillage Res., 64, 101–111, 2002.

GE Healthcare: MicroView 2.1.2 – MicroCT Visualization and Analysis, London, Canada, pp 315, 2006.

Gibson, J. R., Lin, H., and Bruns, M. A.: A comparison of fractal analytical methods on 2- and 3-dimensional computed tomographic scans of soil aggregates, Geoderma, 134, 335–348, 2006.

Giménez, D., Allmaras, R. R., Huggins, D. R., and Nater, E. A.: Mass, surface and fragmentation fractal dimensions of soil fragments produced by tillage, Geoderma, 86, 261–278, 1998.

Giménez, D., Allmaras, R. R., Nater, E. A., and Huggins, D. R.:. Fractal dimensions for volume and surface of interaggregate pores – scale effects, Geoderma, 77, 19–38, 1997.

Grevers, M. C. J. and de Jong, E.: Evaluation of soil-pore continuity using geostatistical analysis on macroporosity in serial sections obtained by computed tomography scanning, in: Tomography of soil-water-root processes, edited by: Anderson, S. H. and Hopmans, J. W., p. 73–86, SSSA Spec. Bub., 36, SSSA, Madison, WI, 1994.

Lovejoy, S., Schertzer, D., and Tsonis, A. A.: Functional Box-Counting and Multiple Elliptical Dimensions in Rain, Science,

235, 1036–1038, 1987.

Melo, F. J. R. and dos Santos, M. C.: Micromorfologia e mineralogia de dois solos de Tabuleiro costeiro de Pernambuco, R. bras. Ci. Solo, 20, 99–108, 1996.

Oleschko, K.: Delesse principle and statistical fractal sets: 1. Dimensional equivalents, Soil Tillage Res., 49, 255–266, 1998.

Oleschko, K., Fuentes, C., Brambila, F., and Alvarez, R.: Linear fractal analysis of three Mexican soils in different management systems, Soil Technol., 10, 207–223, 1997.

Oleschko, K., Brambila, F., Aceff, F., and Mora, L. P.: From fractal analysis along a line to fractals on the plane, Soil Tillage Res., 45, 389–406, 1998.

Origin Lab Corporation: Origin Pro 7.5, Northampton, MA, pp 257, 2006.

Pachepsky, Y. A., Yakovchenko, V., Rabenhorst, M. C., Pooley, C., and Sikora, L. J.: Fractal parameters of pore surfaces as derived from micromorphological data: effect of long term management practices, Geoderma, 74, 305–319, 1996.

Perret, J. S., Prasher, S. O., Kantzas, A., and Langford, C.: 3D visualization of soil macroporosity using X-ray CAT scanning, Can. Agric. Eng. J., 39, 249–261, 1997.

Perret, J. S., Prasher, S. O., Kantzas, A., and Langford, C.: Characterization of macropore morphology in a sandy loam soil using X-ray computer assisted tomography and geostatistical analysis, Can. Water Resou. J., 23, 143–166, 1998.

Perret, J., Prasher, S. O., Kantzas, A., and Langford, C.: Three-Dimensional Quantification of Macropore Networks in Undisturbed Soil Cores, Soil Sci. Soc. Am. J., 63, 1530–1543, 1999.

Perret, J. S., Prasher, S. O., and Kacimov, A. R.: Mass fractal dimension of soil macropores using computed tomography: from box-counting to the cube-counting algorithm, European J. Soil Sci., 54, 569–579, 2003.

Perrier, E., Tarquis, A. M., and Dathe, A.: A Program for Fractal and Multifractal Analysis of Two-Dimensional Binary Images. Computer Algorithms versus Mathematical Theory, Geoderma, 134, 284–294, 2006.

Peyton, R. L., Gantzer, C. J., Anderson, S. H., Haeffner, B. A., and Pfeifer, P.: Fractal dimension to describe soil macropore structure using X ray computed tomography, Water Resour. Res., 30, 691–700, 1994.

Pierret, A., Capowiez, Y., Belzunces, L., and Moran, C. J.: 3D reconstruction and quantification of macropores using X-ray computed tomography and image analysis, Geoderma, 106, 247–271, 2002.

Rasband, W.: ImageJ 1.36, National Insitutes of Health, USA, 153 pp, 2006.

Rasiah, V. and Aylmore, L. A. G.: Estimating microscale spatial distribution of conductivity and pore continuity using computed tomography, Soil Sci. Soc. Am. J., 62, 1197–1202, 1998a.

Rasiah, V. and Aylmore, L. A. G.: Characterizing the changes in soil porosity by computed tomography and fractal dimension, Soil Sci., 163, 203–211, 1998b.

Rachman, A., Anderson, S. H., and Gantzer, C. J.: Computed-Tomographic Measurement of Soil Macroporosity Paramenters as Affected by Staff-Stemmed Grass Hedges, Soil Sci. Soc. Am. J., 69, 1609–1616, 2005.

Rogasik, H., Crawford, J. W., Wendroth, O., Young, I. M., Joshko, M., and Ritz, K.: Discrimination of soil phases by dual energy X-ray tomography, Soil Sci. Soc. Am. J., 63, 741–751, 1999.

Saucier, A.: Effective permeability of multifractal porous media, Physica A, 183, 381–397, 1992.

Tarquis, A. M., Giménez, D., Saa, A., Díaz, M. C., and Gascó, J. M.: Scaling and Multiscaling of Soil Pore Systems Determined by Image Analysis, in: Scaling Methods in Soil Physics, edited by: Pachepsky, Y. A., Radcliffe, D. E., and Selim, H. M. E., CRC Press, 434 pp, 2003.

Tel, T. and Vicsek, T.: Geometrical multifractality of growing structures, J. Phys. A, General, 20, L835–L840, 1987.

Warner, G. S., Nieber, J. L., Moore, I. D., and Geise, R. A.: Characterizing macropores in soil by computed tomography, Soil Sci. Soc. Am. J., 53, 653–660, 1989.

Zeng, Y., Gantzer, C. J., Payton, R. L., and Anderson, S. H.: Fractal Dimension and Lacunarity of Bulk Density Determined with X-ray Computed Tomography, Soil Sci. Soc. Am. J., 60, 1718–1724, 1996.